Chemical Science

ROYAL SOCIETY OF CHEMISTRY

EDGE ARTICLE

View Article Online
View Journal | View Issue



Cite this: *Chem. Sci.*, 2024, **15**, 19359

All publication charges for this article have been paid for by the Royal Society of Chemistry

# A high entropy metallic–high entropy nonmetallic community as a high performance electrocatalyst for the oxygen evolution reaction and oxygen reduction reaction†

Chunyan Zhang,[a] Hang Li,[a] Mengfei Su,[a] Shengfa Li,[a] Feng Gao *[b] and Qingyi Lu *[a]

Received 8th August 2024
Accepted 19th October 2024

DOI: 10.1039/d4sc05326e

rsc.li/chemical-science

The multi-element synergism in high-entropy materials (HEMs) provides great opportunities as multi-functional catalysts or for the promotion of tandem reactions. Herein, a strategy that utilizes a high entropy precursor is proposed to realize the formation of a unique high entropy metallic–high entropy non-metallic community (HEM–HENMC). Aminotriazole acts as a "bonding agent" for the high entropy precursor, and not only binds the five metals Cr, Mn, Fe, Co and Ni together, but also introduces nitrogen and carbon *in situ*. After simultaneous phosphorization and vulcanization and surface oxidation, the unique HEM–HENMC containing five metals (Cr, Mn, Fe, Co and Ni) and five non-metals (C, N, O, P and S) was successfully prepared. The synergistic effect of the various non-metal and metal ions imparts the HEM–HENMC with excellent electrochemical activity. When used as an OER electrocatalyst, the HEM–HENMC exhibits a low overpotential of 211.9 mV (@10 mA $cm^{-2}$) and has excellent stability for over 25 h, while as an ORR electrocatalyst, a satisfactory initial voltage of 0.977 V, half wave potential of 0.841 V and excellent 25 h electrochemical stability are achieved. This work provides an important research basis for the development of high entropy metallic–high entropy nonmetallic materials.



## Introduction

The oxygen reduction/oxygen evolution reaction (ORR/OER) is a key reaction in many energy storage and conversion applications, including metal–air cells, fuel cells, and electrolytic cells.[1–3] To date, a great deal of research has been conducted on the development of efficient catalysts for the ORR and OER. Pt, Ir and other noble metal-based catalysts currently offer the best all-round performances, but their high cost and poor durability obstructs their sustainable utilization across the energy sector.[4] Therefore, developing efficient, durable and low-cost electrocatalysts is very important for energy storage and conversion applications, by either increasing the initial and half wave potentials in the ORR or by decreasing the overpotential in the OER.[5] Transition metal-based catalysts have recently emerged as promising candidates to fill this role due to their good electrical conductivity and potentially good activity.[6,7] However, transition metal sulfide/phosphide compounds have poor stability under high oxidation electrochemical conditions, for example, they show thermodynamic instability, undergo structural and morphological deformation, and suffer from catalyst detachment from the substrate.[8] Therefore, the design of a transition metal-based catalyst with high catalytic activity and excellent stability is the focus of current research in the field of catalysis. One approach to create such novel materials is to increase their chemical complexity.

High entropy materials (HEMs) contain at least five metallic elements uniformly mixed into solid solutions, providing great opportunities for materials discovery, performance optimization, and advanced applications.[9] For example, the compositional flexibility of HEMs allows the fine-tuning of catalytic activity and selectivity, whilst the multi-element synergies in HEMs provide a different range of adsorption sites and are ideal for multistep tandem reactions or reactions requiring multi-functional catalysts.[10] In 2004, Yeh and Cantor almost simultaneously proposed the concept of high entropy alloys (HEAs).[11,12] The "four core effects" including high entropy effects, lattice distortion effects, slow diffusion effects and "cocktail" effects give HEAs excellent properties and broad application prospects in mechanics, magnetism, catalysis and

[a]*State Key Laboratory of Coordination Chemistry, Coordination Chemistry Institute, Collaborative Innovation Center of Advanced Microstructures, School of Chemistry and Chemical Engineering, Nanjing University, Nanjing 210023, P. R. China. E-mail: qylu@nju.edu.cn*

[b]*Department of Materials Science and Engineering, Jiangsu Key Laboratory of Artificial Functional Materials, Collaborative Innovation Center of Advanced Microstructures, College of Engineering and Applied Sciences, Nanjing University, Nanjing 210023, P. R. China. E-mail: fgao@nju.edu.cn*

† Electronic supplementary information (ESI) available. See DOI: https://doi.org/10.1039/d4sc05326e

other fields.[13] As a result of the in-depth study of HEMs, the types of known high entropy nanomaterials have rapidly developed from metal alloys to intermetallics, oxides, sulfides and others.[14–17] Although high entropy compounds or HEAs have achieved some excellent results in the field of electrocatalysis, to synthesize high entropy compounds in a simple, efficient and high-quality manner remains a daunting task for the research community.[18] Furthermore, studies of HEMs have mostly focused on high entropy metallic oxides with only a few on high entropy metallic phosphides and sulfides. In contrast to high-entropy metallic compounds, high-entropy nonmetallic systems have rarely been reported. But in fact, compounds containing the same metal but different anions (*e.g.*, C, N, O, P, and S) show different electrochemical properties, and the addition of one or more anions can effectively change their physical or electronic structure to positively enhance the properties by increasing the number of active sites,[19] enhancing the stability,[20] tuning the energy barrier,[21] and by other effects.[4,22] Therefore, as another type of high entropy system, we put forward the concept of the high entropy nonmetal system. Tuning the catalyst–adsorbate interactions *via* multiple-elemental synergies to adjust the charge state in multi-metal compound holds much promise for enhancing catalytic activity. High entropy nonmetallic ions also have certain advantages over high entropy metal nanomaterials and are worth further exploration.

Herein, a new concept of a "high entropy metallic–high entropy nonmetallic community" (HEM–HENMC) is proposed to design a high efficiency electrochemical catalyst. The designed electrochemical catalyst contained five metals, Fe, Co, Ni, Mn, and Cr, and five non-metals, C, N, O, P, and S, and can be produced through a high entropy precursor strategy. The high entropy metallic precursor is obtained by a simple solvothermal method with aminotriazole acting as a "bonding agent" to not only bind together the five metal species (Fe, Co, Ni, Mn and Cr), but also introduce nitrogen and carbon at the same time. The subsequent simultaneous phosphorization and vulcanization of the high entropy precursor successfully introduces S and P, while surface oxidation achieves the introduction of O. Therefore, a special HEM–HENMC with the co-existence of ten elements (five metals, Fe, Co, Ni, Mn, and Cr and five non-metals, C, N, O, P, and S) is successfully obtained. When used as an OER electrocatalyst, the HEM–HENMC exhibits a low overpotential of 211.9 mV (@10 mA $cm^{-2}$), along with excellent stability over 25 h without any overpotential increase. Moreover, a satisfactory initial voltage of 0.977 V, a half wave potential of 0.841 V and an excellent 25 h electrochemical stability are achieved in the ORR test. The outstanding electrochemical activities of the HEM–HENMC can be attributed to the synergistic interaction of the five metallic elements and five non-metallic ones, and provides a new way of thinking for the study of high entropy materials.

## Results and discussion

In this study, the synthesis of the high entropy metallic–high entropy nonmetallic community (HEM–HENMC) is achieved through a very simple precursor method, as shown in Fig. 1a. During the solvothermal synthesis of the precursor, aminotriazole is used to bind five kinds of metals (Fe, Co, Ni, Mn and Cr) together to form a spherical high entropy precursor. The use of aminotriazole not only integrates the five kinds of metals together, but also introduces nitrogen and carbon *in situ*, which lays a foundation for the HEM–HENMC synthesis. In addition, solvothermal treatment always leads to surface oxidation and thus introduces oxygen to the precursor so that a high entropy precursor containing C, N and O is successfully prepared. In order to synthesize compounds containing more nonmetallic ions, an upstream gas method is employed and a simultaneous phosphorization and vulcanization of the high entropy precursor is carried out to introduce sulfur and phosphorus elements into the product. Compared with a previous $M_xS_y$ material containing only one metal element and one non-metal element, we make unprecedented progress in introducing five

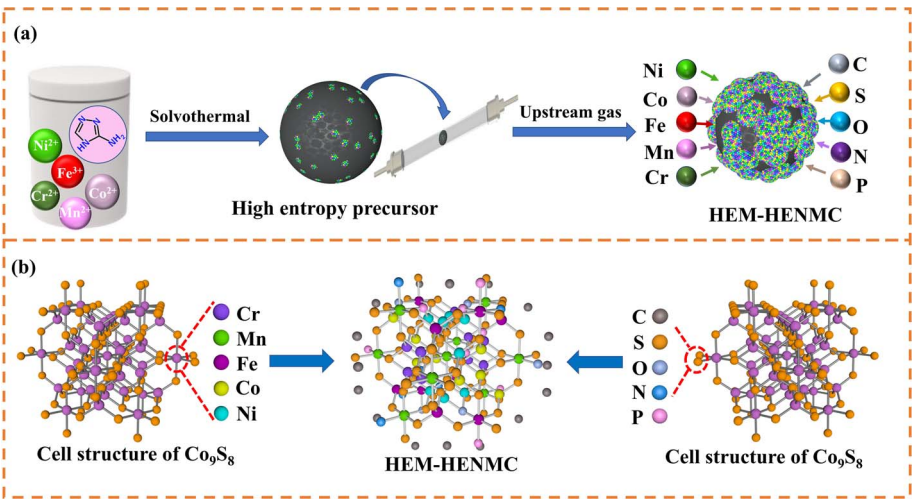


Fig. 1 (a) Schematic illustration of the formation process of the HEM–HENMC. (b) The metallic elements Cr, Mn, Fe, Co, and Ni occupy the cation positions, and the non-metallic elements N, O, P, and S occupy the anion positions in the sulfide cell to form the HEM–HENMC.

metals to occupy the cation positions and different anions (N, O, P, and S) to occupy the anion positions in the sulfide cell structure with a carbon coating around the material, as shown in Fig. 1b. Thus, a high entropy metallic–high entropy nonmetallic community (HEM–HENMC) is formed.

It is well known that HEMs exhibit excellent activity and stability in catalysis due to their inherent synergistic effects and high entropy.[23] Of course, the morphology and composition of HEMs also play a very important role. Scanning electron microscopy (SEM, Fig. S1, ESI†) and transmission electron microscopy (TEM, Fig. 2a) were used to explore the morphologies of the synthesized HEM–HENMC. It can be seen that the HEM–HENMC has a spherical structure with sizes in the range of 100–200 nm. As a catalyst, the spherical structure of the material has the advantages of a large effective specific surface area, stable structure and small size which is conducive to charge transfer and ion transport. Fig. 2b and S2† show high-resolution TEM (HRTEM) images of a single sphere, indicating that the HEM–HENMC spheres are composed of many nanoparticles with sizes of about 5 nm. Lattice spacings of 0.301 nm, 0.192 nm and 0.176 nm which correspond to the (311), (511) and (440) facets of cubic $Co_9S_8$, respectively, can be easily detected and can be further verified in the corresponding selected area electron diffraction (SAED) pattern in Fig. 2c. Scanning TEM energy-dispersive X-ray spectroscopy (STEM-EDX) elemental mapping was employed to demonstrate the presence of 10 elements, as shown in Fig. 2d–m. As can be seen from the figures, the five metals, Cr, Mn, Fe, Co and Ni, are evenly distributed in the sample, and the five non-metals, C, N, O, P and S, are also detected. In order to introduce nitrogen and carbon elements into the structure of the HEM–HENMC, aminotriazole is used as "bonding agent" to prepare high entropy metal precursors *via* a solvothermal method. In addition, the selection of a solvothermal method also has the advantage that oxygen can be easily introduced into the system during this process. *Via* the process of simultaneous phosphorization and vulcanization of the high entropy metal precursor, phosphorus and sulfur are successfully introduced into the high entropy nonmetallic system. Astonishingly, the locations where the phosphorus and sulfur elements are distributed are different. The sulfur is distributed with the metals, which proves the formation of metal–sulfide bonds, while the phosphorus not only forms metal–phosphorus bonds, but also forms nonmetallic bonds with carbon, nitrogen and oxygen, which effectively demonstrates the existence of high entropy nonmetallic parts of the materials and will greatly improve the application range and performances. Similarly, the EDX mappings for the quaternary (MnFeCoNi)-high entropy nonmetal system and ternary (FeCoNi)-high entropy nonmetal system are shown in Fig. S3,† indicating that ternary and quaternary metallic high entropy nonmetallic communities were also successfully achieved.

The valence states of the metallic elements were examined and X-ray photoelectron spectroscopy (XPS) was performed to compare the HEM–HENMC with the quaternary (MnFeCoNi)-high entropy nonmetal system and ternary (FeCoNi)-high entropy nonmetal system (Fig. 3a–d and S4a–d†). The survey XPS spectrum is shown in Fig. 3a, from which it can be seen that

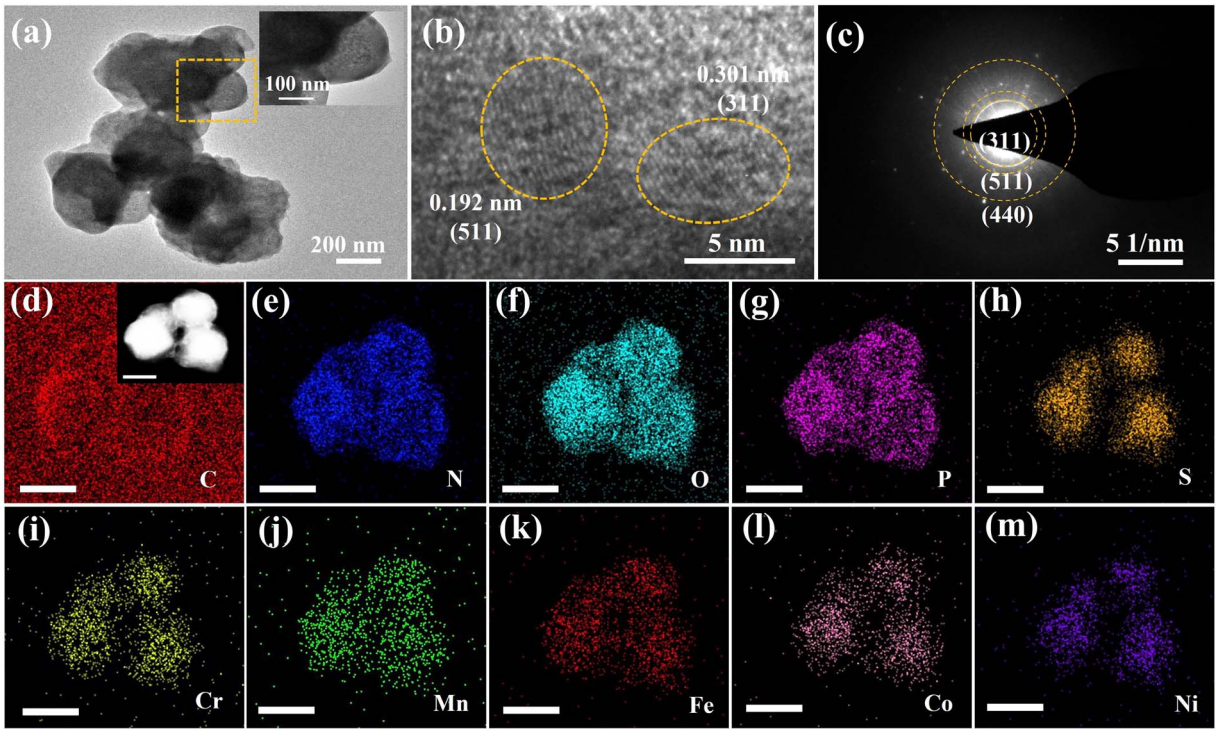


Fig. 2 Structural characterization of the HEM–HENMC nanoparticles: (a) TEM image (inset is the enlarged image of the box); (b) HRTEM image; (c) SAED pattern and (d–m) STEM-EDX elemental mappings, the scale bars are 100 nm.

all the 10 elements including five metals (Cr, Mn, Fe, Co and Ni) and five non-metals (C, N, O, P and S) can be detected, further confirming the formation of the HEM–HENMC. Fig. 3b shows the high-resolution Mn 2p XPS spectrum, in which the peaks centered at 641.86 eV and 653.05 eV are arisen by Mn $2p_{3/2}$ and Mn $2p_{1/2}$ of $Mn^{2+}$ whereas the peaks at 645.40 eV and 655.43 eV are related to Mn $2p_{3/2}$ and Mn $2p_{1/2}$ of $Mn^{3+}$.[24,25] Both the Mn $2p_{3/2}$ and Mn $2p_{1/2}$ peaks positively shift to higher binding energies when compared to the quaternary(MnFeCoNi)/ternary(FeCoNi) metallic–high entropy nonmetallic systems, as shown in Fig. S4a.† In Fig. 3c, the Fe $2p_{3/2}$ and Fe $2p_{1/2}$ peaks with binding energies of 708.21 and 721.02 eV indicate the

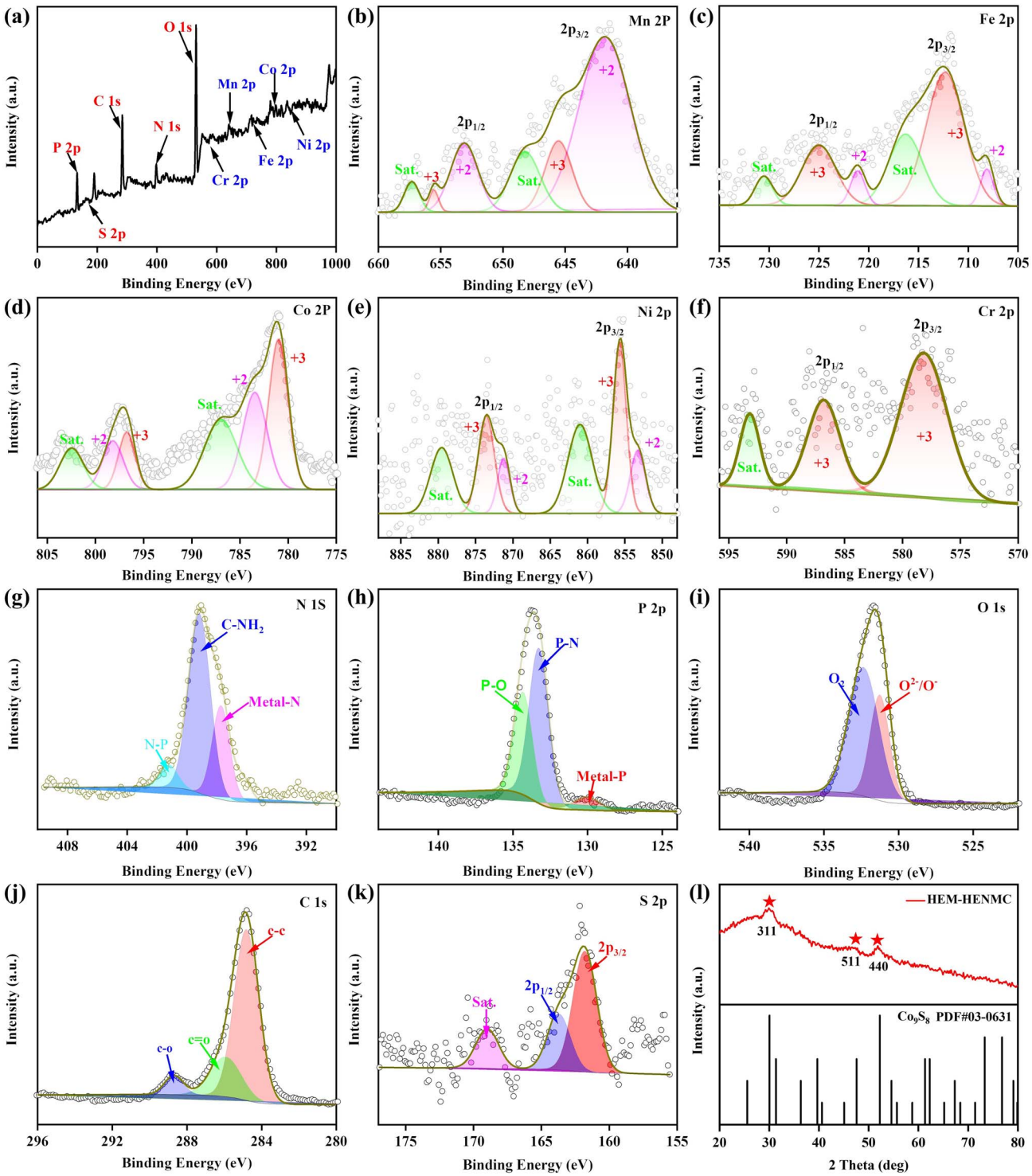


Fig. 3 (a) Full XPS survey spectrum; (b–k) high-resolution XPS spectra of (b) Mn 2p, (c) Fe 2p, (d) Co 2p, (e) Ni 2p, (f) Cr 2p, (g) N 1s, (h) P 2p, (i) O 1s, (j) C1s and (k) S 2p for the HEM–HENMC; and (l) XRD pattern of the HEM–HENMC.

existence of $Fe^{2+}$ in the HEM–HENMC, while those at 712.36 and 724.98 eV reveal the existence of $Fe^{3+}$.[26] As shown in Fig. S4b,† the Fe $2p_{3/2}$ peaks of the HEM–HENMC shift to higher binding energies when compared to those of the quaternary(MnFeCoNi)/ternary(FeCoNi) metallic–high entropy nonmetallic system, which indicates that the Fe in the HEM–HENMC exists in an electron-deficient state. Conversely, compared with the quaternary(MnFeCoNi)/ternary(FeCoNi) metallic–high entropy nonmetallic system, the Co 2p peaks of the HEM–HENMC shift to lower binding energies, implying that the Co exists in an electron-rich state (Fig. S4c†).[16] In Fig. 3d of the Co 2p XPS spectrum, the peaks at around 781.18 eV and 796.68 eV are related to Co $2p_{3/2}$ and Co $2p_{1/2}$, respectively. The spin–orbit doublets situated at 783.58 and 798.18 eV can be ascribed to $Co^{2+}$, and those at 781.08 and 796.85 eV correspond to the spin–orbit splitting of $Co^{3+}$.[27,28] The intensity of the peaks indicates that $Co^{3+}$ is the dominant state of Co near the surface of the HEM–HENMC sample, which is consistent with previous reports.[16] Similarly, in the Ni 2p XPS spectrum of the HEM–HENMC (Fig. 3e), the peaks at 875.0 eV and 888.0 eV belong to the $2p_{3/2}$ and $2p_{1/2}$ peaks of $Ni^{2+}$, while the peaks at 857.4 eV and 877.6 eV correspond to $Ni^{3+}$. Two additional satellite peaks at 861.9 eV and 881.7 eV are also observed.[29–31] Meanwhile, the $Ni^{3+}$ $2p_{3/2}$ peak appears at a lower binding energy in contrast with the quaternary(MnFeCoNi)/ternary(FeCoNi) metallic–high entropy nonmetallic system (Fig. S4d†). As shown in Fig. 3f, the Cr 2p XPS spectrum can be fitted into three peaks, of which the two at 578.19 and 586.89 eV are ascribed to Cr $2p_{3/2}$ and Cr $2p_{1/2}$ of $Cr^{3+}$, respectively.[15,32] The peak shifts in the Fe, Co, Ni, and Mn spectra imply that Fe and Mn serve as electron donors to Co and Ni, indicating a synergy effect among the metal species which would be beneficial to oxygen electrocatalysis reactions such as the OER.

It is also important to study the chemical state of the nonmetallic elements in the HEM–HENMC. The high-resolution N 1s, P 2p, O 1s, S 2p, and C 1s XPS spectra of the HEM–HENMC are displayed in Fig. 3g–k. The high-resolution N 1s XPS spectrum in Fig. 3g shows the presence of three peaks, which are assigned to the N–metal (398.3 eV), C–$NH_2$ (399.6 eV), and N–P (401.5 eV) species.[33–35] In recent years, heterogeneous catalysts with M–$N_x$ sites (M = Fe, Co, Ni, *etc.*) on carbon supports have emerged as promising catalysts. N-doped metallic compounds have the key advantages of high metal atom utilization efficiency, high intrinsic activity, and low cost.[36,37] Therefore, the nitrogen introduced from aminotriazole forms metal–N bonds and also facilitates nitrogen doping during the simultaneous phosphorization and vulcanization process, both of which would positively promote the catalytic performance of the material. The doped nitrogen in the HEM–HENMC has a larger negative charge density than the metal ions, resulting in a higher positive charge density of other atoms in its vicinity, improving the chemisorption of $O_2$, and thus increasing the mobility of the electrons and catalytic reaction efficiency.[38] The P 2p high resolution XPS spectrum in Fig. 3h can be deconvoluted into five peaks at 130.1, 131.1, 132.2, 133.2, and 134.2 eV, and are caused by the P $2p_{3/2}$ and P $2p_{1/2}$ peaks of the metal phosphides, and the formation of P–metal, P–N, and P–O bonds, respectively.[4,22,39] The P–O peak should originate from the oxidized P species while the P–N peak results from the process of simultaneous phosphorization and vulcanization. The XPS results confirm that some P has been doped into the carbon/nitrogen matrix during the high temperature decomposition of aminotriazole to form C–P/N–P bonds, thus adjusting the electronic structure and surface polarity of the high entropy transition metal components, enhancing the electronic interaction and electrical conductivity of the HEM–HENMC, and thereby facilitating the improvement of the related electrocatalytic performance.[40] This is further demonstrated by O 1s and C 1s XPS spectra in Fig. 3i and j, respectively. The O 1s spectrum displays a peak corresponding to $O^{2-}/O^{-}$ with a binding energy at 531.5 eV and a peak corresponding to $O_2$ with a binding energy at 533.8 eV, which could come from ambient air.[41,42] The C 1s XPS spectrum in Fig. 3j can be fitted and divided into three types of carbon bonds: aromatic-linked carbon (C–C, 284.38 eV); oxygen single-bonds carbon (C–O, 285.58 eV) and carbonyl carbon (C=O, 286.68 eV).[43,44] The S 2p narrow scan is shown in Fig. 3k and can be divided into two peaks at 163.68 and 162.08 eV corresponding to S $2p_{1/2}$ and S $2p_{3/2}$,[45] respectively, further proving that high entropy transition metal sulfides were successfully prepared using this simple method. The X-ray diffraction (XRD) pattern of the HEM–HENMC is displayed in Fig. 3l. The major diffraction peaks of the HEM–HENMC could be indexed to the (311), (511), and (440) planes of standard $Co_9S_8$ (PDF#03-0631). This result shows that multiple metals replace some of the Co while multiple nonmetals replace some of S in the lattice of the $Co_9S_8$ to create a single-phase HEM–HENMC instead of individual binary sulfides.[16,46] The anions coordinate with each other, change the surface structure, and increase the utilization efficiency of the material, thus resulting in a great improvement in the catalytic performance.

The electrocatalytic OER properties of the as-prepared HEM–HENMC were evaluated using a typical three-electrode system in a 1.0 M KOH electrolyte solution. A glassy carbon electrode deposited with the catalyst, Hg/HgO and graphite are used as the working electrode, the reference electrode, and the counter electrode, respectively. In order to explore the influence of the high entropy nonmetals in the HEM–HENMC on the material properties, the OER performance was tested for the materials containing the five metals but with different anions, as shown in Fig. 4a. For uniform nomenclature, the HEM–HENMC is designated as (CrMnFeCoNi)–P/S in the following expressions, unless specifically mentioned. In the experiments, different treatments of the same precursor can result in catalysts containing different anions, which are described in detail in the experimental section and Table S1.† In order to investigate whether the structure of the obtained samples under different treatment conditions was changed, the samples were characterized using TEM and EDS. Fig. S5† displays the TEM images of the samples. It can be observed that the structure of the four catalyst samples is not significantly different from that of the HEM–HENMC (Fig. 2a). Fig. S6–S9† show the EDS elemental mappings of (CrMnFeCoNi)–P, (CrMnFeCoNi)–$N_2$, (CrMnFeCoNi)–S, and (CrMnFeCoNi)–$O_2$, showing that not only the five

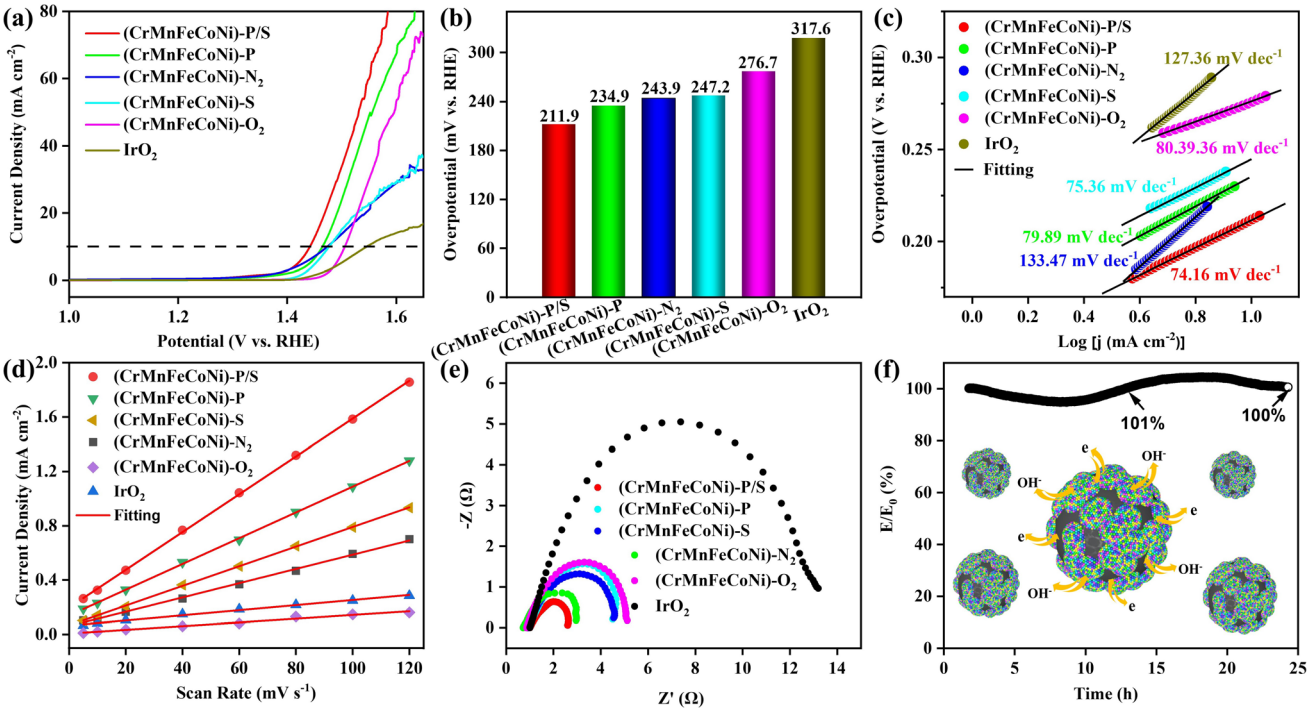


Fig. 4 OER performance: (a) LSV curves; (b) overpotentials at 10 mA $cm^{-2}$; (c) Tafel slopes; (d) the current density against scan rates for estimating $C_{dl}$ values and (e) EIS spectra of the (CrMnFeCoNi)–P/S, (CrMnFeCoNi)–P, (CrMnFeCoNi)–$N_2$, (CrMnFeCoNi)–S, (CrMnFeCoNi)–$O_2$ and $IrO_2$ electrodes. (f) Long-time stability test of the HEM–HENMC at 20 mA $cm^{-2}$ for 25 h.

metal ions are uniformly distributed on the surface of the samples but also the various anions too. It turns out that although the samples are obtained under different synthetic conditions, their structures do not change significantly. All the potentials obtained by the electrochemical workstation tests were calibrated with respect to the RHE and corrected with 94% *iR*-compensation unless otherwise specified (Fig. S10†). According to the test results, (CrMnFeCoNi)–P/S presents an ultralow overpotential of 211.9 mV@10 mA $cm^{-2}$ as compared to $IrO_2$ (317.6 mV), which is a common criterion against which OER activity is evaluated, suggesting that (CrMnFeCoNi)–P/S has excellent OER performance. For the (CrMnFeCoNi)–$O_2$ sample, which is obtained after direct calcination in oxygen, the only anion in the obtained five-membered metal nanomaterial is oxygen. OER tests show that when the current density is 10 mA $cm^{-2}$, (CrMnFeCoNi)–$O_2$ exhibits an overpotential of 276.7 mV. The anions contained in the samples obtained after vulcanization and calcination under a nitrogen atmosphere are sulfur, carbon, nitrogen and oxygen ((CrMnFeCoNi)–S), and carbon, nitrogen and oxygen ((CrMnFeCoNi)–$N_2$), respectively. In the OER tests, when the current density is 10 mA $cm^{-2}$, the two nanomaterials have similar overpotentials of 247.2 mV and 243.9 mV. Compared with (CrMnFeCoNi)–$O_2$, the overpotential is about 30 mV lower at the same current density, indicating that an increase in the number of anions present in the material promotes the improvement of the OER performance. Similarly, when the phosphorization material ((CrMnFeCoNi)–P) is tested as the OER electrocatalyst, it shows a low overpotential of 234.9 mV@10 mV $cm^{-2}$. The overpotentials of these catalysts are listed in Fig. 4b. As displayed in Fig. 4b, it can be visually observed that the HEM–HENMC ((CrMnFeCoNi)–P/S) displays the best OER performance with the lowest overpotential of 211.9 mV@10 mA $cm^{-2}$, much lower than those of (CrMnFeCoNi)–P (234.9 mV), (CrMnFeCoNi)–$N_2$ (243.9 mV), (CrMnFeCoNi)–S (247.2 mV), (CrMnFeCoNi)–$O_2$ (276.7 mV) and $IrO_2$ (317.6 mV). The different electrocatalytic performances of the catalysts obtained following different high temperature treatments of the same high entropy metal precursor are no doubt due to the existence of different anions in the resulting materials. The anions affect the free energy around the active sites, and the presence of multiple anions increases the disorder of the catalyst structure system, thus changing the adsorption energy of the catalyst. Moreover, transition metal phosphides possess good conductivity, variable compositions, and tunable hydroxyl or water molecule bonding ability, which makes them promising materials for electrocatalysis. Thus, the high entropy transition metal sulfide material doped with N and P displays a stronger electron-rich area around the Fermi level, resulting in higher electronic conductivity and enhanced catalytic performance.[39,47]

It can be seen from the above results that of the five-metal compounds, the nanomaterial containing five anions shows the best OER performance, because the five anions have a synergistic effect to promote each other to improve the electrochemical performance. From the obtained LSV curves, the Tafel slopes in a current density range of 3.15–12.5 mA $cm^{-2}$ were plotted, where a lower Tafel slope means faster OER reaction kinetics.[48] As represented in Fig. 4c, the Tafel slopes of

(CrMnFeCoNi)–P/S, (CrMnFeCoNi)–P, (CrMnFeCoNi)–$N_2$, (CrMnFeCoNi)–S and (CrMnFeCoNi)–$O_2$ are evaluated as 74.16, 79.89, 133.47, 75.36, and 80.39 mV $dec^{-1}$, respectively. For comparison, the commercial $IrO_2$ has a Tafel slope of 127.36 mV $dec^{-1}$. All the results reveal that (CrMnFeCoNi)–P/S has the lowest Tafel slope and the fastest OER reaction kinetics, further demonstrating the advantages of the HEM–HENMC. To further probe the electrochemical properties of the catalysts, the electrochemical active surface area (ECSA) values of the samples were estimated by examining the electrical-double layer capacitance ($C_{dl}$), as illustrated in Fig. 4d, while the CV curves used to calculate the $C_{dl}$ are shown in Fig. S11.† Accordingly, the largest ECSA of the investigated electrocatalysts is that of (CrMnFeCoNi)–P/S with a value of 34.75 $cm^2$. This value is much higher than those of (CrMnFeCoNi)–P (23.83 $cm^2$), (CrMnFeCoNi)–$N_2$ (18.20 $cm^2$), (CrMnFeCoNi)–S (13.75 $cm^2$), (CrMnFeCoNi)–$O_2$ (3.18 $cm^2$) and $IrO_2$ (4.48 $cm^2$). The ECSA evaluation provides a better understanding of the effects that the intrinsic interactions of the metallic and nonmetallic elements in the community structure have on the electrochemical properties. The ECSA test results show that the active surface of the HEM–HENMC electrode is the largest and can participate in the electrochemical reaction.[49] In the HEM–HENMC catalyst, there are five nonmetals that work together, resulting in increased disorder in the material and thus increasing catalytic activity. In short, the high entropy materials containing different kinds of nonmetallic ions have different electrochemical activities, which proves that the study of high entropy nonmetallic materials has far-reaching significance in the field of electrochemistry.

Electrochemical impedance spectroscopy (EIS) was utilized to elucidate the charge transfer and capacitive processes within various electrochemical systems. In this regard, the superior conductivity of the HEM–HENMC (CrMnFeCoNi)–P/S is confirmed *via* EIS analysis, as shown in Fig. 4e, with a charge transfer resistance of around 2.5 Ω that is lower than those of (CrMnFeCoNi)–$N_2$ (3.0 Ω), (CrMnFeCoNi)–P (4.5 Ω), (CrMnFeCoNi)–S (4.5 Ω), (CrMnFeCoNi)–$O_2$ (5.3 Ω) and $IrO_2$ (13.9 Ω). More importantly, the (CrMnFeCoNi)–P/S also exhibits long-term stability without obvious degradation of the current density at 1.45 V for nearly 25 h, as analyzed using chronoamperometry under OER conditions. As shown in Fig. 4f, after 25 h of measurement, 100% of the initial current density is maintained. In addition, it should be mentioned that the wavy trend seen in the test curve in Fig. 4f may be caused by the large temperature difference between day and night. In order to further explore the stability of the HEM–HENMC at a higher current density, the OER stability test was carried out at around 60 mA $cm^{-2}$ for 24 hours. As shown in Fig. S12,† the catalytic stability of the HEM–HENMC is satisfactory even at high current density and after 24 hours and the voltage retention rate is 93.86%. The slight jitter in the curve after 12 hours is due to the effect of the generated gas on the collection of the current signal at high current density.

The electrocatalytic OER activity of the quinary-metal (CrMnFeCoNi)–P/S is remarkably competitive and even shows superior performance to that of commercial $IrO_2$, demonstrating the state-of-the-art nature of the synthesized (CrMnFeCoNi)–P/S nanoparticles. To evaluate the effect of the high entropy metals on the OER performances, ternary (FeCoNi)–P/S, and quaternary (MnFeCoNi)–P/S were tested as control groups. Fig. 5a shows the linear sweep voltammetry (LSV) curves of (CrMnFeCoNi)–P/S, (MnFeCoNi)–P/S, and (FeCoNi)–P/S. (CrMnFeCoNi)–P/S exhibits an overpotential of 206 mV to reach a current density of 10 mA $cm^{-2}$, which is 26 and 48 mV lower than those of (MnFeCoNi)–P/S and (FeCoNi)–P/S, respectively. The specific values of the overpotential in the OER test at a current density of 10 mA $cm^{-2}$ are shown in Fig. 5b, clearly revealing the positive effect the cocktail of metals have on the OER performance. To further demonstrate that the catalytic performance of the HEM–HENMC is repeatable, we tested 20 different batches of the HEM–HENMC. The results show that the overpotential of the HEM–HENMC at 10 mA $cm^{-2}$ can be stabilized in the range of 193–225 mV (Fig. S13†). The Tafel slope of (CrMnFeCoNi)–P/S derived from the LSV curve is about 74.17 mV $dec^{-1}$, smaller than those of (MnFeCoNi)–P/S (75.19 mV $dec^{-1}$) and (FeCoNi)–P/S (78.84 mV $dec^{-1}$), as shown in Fig. 5c. In general, a smaller Tafel slope within a reasonable range infers faster kinetics based on a similar mechanism. Thus, the Tafel analysis supports the superior activity of our (CrMnFeCoNi)–P/S catalyst for the OER. A comparison of the OER performance in our work and recently reported transition metal compounds can be found in Table S2.† The enhanced OER activity of the quinary metal system is attributed to the fact that, compared with the ternary and quaternary metal systems, the Mn and Fe act as electron donors to make the Co and Ni more electron rich, thus improving the activity of the electrocatalyst.[50,51] The results of the EIS tests for (CrMnFeCoNi)–P/S, (MnFeCoNi)–P/S, and (FeCoNi)–P/S shown in Fig. S14† further reveals the higher conductivity of (CrMnFeCoNi)–P/S. The OER activity increases with the number of metal elements present in the material, and the synergistic effect of multiple metal ions can adjust the electronic structure to regulate the optimal catalyst–adsorbent interactions, so that the (CrMnFeCoNi)–P/S nanoparticles have the best electrochemical activity. This explains the synergistic effect between the five anions and the five cations, which is conducive to the improvement of the catalytic performance of the HEM–HENMC. Firstly, the five cations (Cr, Mn, Fe, Co, Ni) and four anions (N, O, P, S) occupy the Co and S positions in the $Co_9S_8$ cell structure, respectively. Due to the different radii of the various anions and cations, lattice distortion is caused, thereby increasing the number of active catalytic sites in the material. Secondly, peak shifts in the spectra of Fe, Co, Ni, and Mn indicate that Fe and Mn become electron donors to Co and Ni, indicating a synergistic effect between the metals that favors oxygen electrocatalysis (Fig. S4†). Finally, the XPS spectra prove that the five nonmetals contain different bonds in the HEM–HENMC. For example, the N forms N–metal (398.3 eV), C–$NH_2$ (399.6 eV), and N–P (401.5 eV) bonds and the P forms P-metal, P–N, and P–O bonds. This shows that interactions exist between the five anions which can adjust the electronic structure and surface polarity of the high entropy transition metal components, thus enhancing the electronic interactions and electrical conductivity of the HEM–HENMC, and thereby facilitating the improvement of the related electrocatalytic performance.

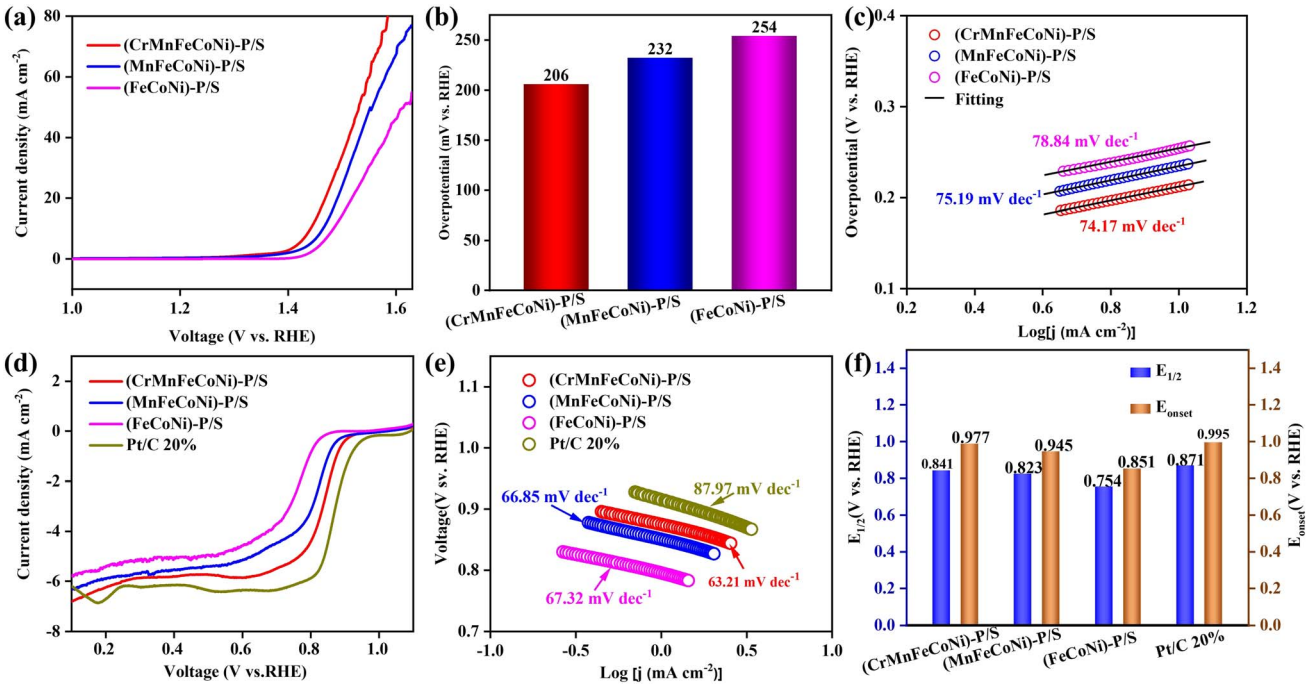


Fig. 5 OER performance. (a) LSV curves; (b) overpotentials at 10 mA $cm^{-2}$ and (c) Tafel slopes of the (CrMnFeCoNi)–P/S, (MnFeCoNi)–P/S, and (FeCoNi)–P/S electrodes. ORR performance. (d) LSV curves, (e) $E_{1/2}$ and $E_{onset}$ (*vs.* RHE) and (f) Tafel slopes of the (CrMnFeCoNi)–P/S, (MnFeCoNi)–P/S, (FeCoNi)–P/S and Pt/C 20% electrodes.

Rotating ring-disk electrode (RRDE) tests were performed to assess the catalytic ORR performance of the as-synthesized catalysts using a typical three-electrode system in 1 M KOH. The cyclic voltammetry (CV) curves show that (CrMnFeCoNi)–P/S exhibits an obvious $O_2$ reduction peak in the $O_2$-saturated electrolyte when compared with that obtained in the $N_2$-saturated solution (Fig. S15†), suggesting that (CrMnFeCoNi)–P/S possesses high intrinsic catalytic activity for the $O_2$ reduction reaction. As shown in Fig. 5d, (CrMnFeCoNi)–P/S delivers an impressive ORR onset potential ($E_{onset}$) of 0.977 V and half wave potential ($E_{1/2}$) of 0.841 V in LSV measurements, outperforming (MnFeCoNi)–P/S (0.945 and 0.823 V, respectively) and (FeCoNi)–P/S (0.851 and 0.754 V, respectively), and delivering values close to those of commercial noble metal materials (Pt/C, 5%, 0.995 and 0.872 V, respectively). The specific values of the initial potential and half wave potentials of the relevant materials are shown in Fig. 5e. The outstanding ORR activity of (CrMnFeCoNi)–P/S is further exemplified by its low Tafel slope of 63.21 mV $dec^{-1}$ (Fig. 5f), which is lower than those of Pt/C (87.97 mV $dec^{-1}$), (MnFeCoNi)–P/S (66.85 mV $dec^{-1}$) and (FeCoNi)–P/S (67.32 mV $dec^{-1}$). The RRDE tests thus verify that (CrMnFeCoNi)–P/S is an outstanding ORR catalyst under alkaline conditions. Hydrogen peroxide ($H_2O_2$) yields during the ORR were investigated using RRDE tests, allowing examination of the ORR pathway. The LSV curves of (CrMnFeCoNi)–P/S at different rotation speeds are shown in Fig. S16.† (CrMnFeCoNi)–P/S shows a $H_2O_2$ yield below 2% over a wide range of potentials, whereas (MnFeCoNi)–P/S and (FeCoNi)–P/S produce much higher $H_2O_2$ yields (Fig. S17†). As calculated from eqn (Se1) and (Se2) in the ESI,† the average electron transfer number for (CrMnFeCoNi)–P/S is ≈3.95 in the potential range from 0.2 to 0.8 V, indicating an unusually high selectivity for oxygen reduction to $OH^-$ *via* a 4-electron pathway. This result is consistent with the calculation results from the Koutecký–Levich (KL) plots (Se3–Se5), where the average electron transfer number for (CrMnFeCoNi)–P/S is close to 4.0 at all potentials studied. In comparison, the control samples, (MnFeCoNi)–P/S and (FeCoNi)–P/S, show inferior selectivity toward the 4-electron ORR pathway. The ORR stability of (CrMnFeCoNi)–P/S was next investigated *via* chronoamperometry tests at a potential of 0.5 V (*vs.* RHE). (CrMnFeCoNi)–P/S exhibits a current retention of 96.16% after 90 000 s test (Fig. S18†), verifying the feasibility of the prepared catalyst for long-term use. Comparison of the ORR performance between the HEM–HENMC and other recently reported transition metal compounds can be found in Table S3,† proving that the HEM–HENMC is one of the best ORR electrocatalysts. In short, the catalysts containing different types of metallic elements and nonmetallic elements show different catalytic properties, and the HEM–HENMC, which contains the most elements, exhibits the best electrochemical activities, indicating that the different metallic and nonmetallic ions increases the disorder of the structure and thus improves the catalytic performance.

## Conclusions

In summary, we synthesized homogeneously mixed and entropy-stabilized HEM–HENMC nanoparticles through a facile high entropy metallic precursor method to overcome the immiscibility limits. The high entropy precursor contains five

metallic elements, Cr, Mn, Fe, Co and Ni, coordinated with aminotriazole, which contains C, N and O, and lays a foundation for the synthesis of high entropy nonmetallic materials. The high entropy nonmetallic system is further achieved by a subsequent simultaneous phosphorization and vulcanization process to introduce P and S. Thus, a unique high entropy metallic–high entropy nonmetallic community of ten elements (five metals, Fe, Co, Ni, Mn, and Cr and five nonmetals, C, N, O, P, and S) is successfully obtained. When tested as an OER catalyst, the as prepared HEM–HENMC with 10 elements demonstrates synergistic effects that achieve good catalytic activity and long durability. In addition, during ORR tests, the HEM–HENMC sample shows satisfactory electrochemical performance consistent with transition metal compounds that do not contain precious metals. The HEM–HENMC offers good potential for application as an electrocatalyst while the synthesis method offers a general approach to expand the compositional space of this class of materials. This study therefore opens up a new door toward synthesizing not only various high entropy metal compounds but also high entropy nonmetal materials for a range of energy and catalysis applications.

## Data availability

The data are available within the article and its ESI.† The data that support the findings of this study are available on request from the corresponding author.

## Author contributions

F. G. and Q. L. conceived and supervised the project. C. Z., H. L., M. S., and S. L. conducted the experiments. C. Z., H. L., M. S., S. L., F. G. and Q. L. analysed the data and contributed to writing the manuscript.

## Conflicts of interest

The authors declare no competing interests.

## Acknowledgements

This work is supported by the National Natural Science Foundation of China (Grant No. 22175084 and 22275082).

## References

1 Q. Liu, M. Ranocchiari and J. A. van Bokhoven, *Chem. Soc. Rev.*, 2022, **51**, 188–236.
2 T. M. Tang, X. Bai, Z. L. Wang and J. Q. Guan, *Chem. Sci.*, 2024, **15**, 5082–5112.
3 P. Kumar, K. Kannimuthu, A. S. Zeraati, S. Roy, X. Wang, X. Y. Wang, S. Samanta, K. A. Miller, M. Molina, D. Trivedi, J. Abed, A. C. Mata, H. Al-Mahayni, J. Baltrusaitis, G. Shimizu, Y. A. Wu, A. Seifitokaldani, E. H. Sargent, P. M. Ajayan, J. G. Hu and M. G. Kibria, *J. Am. Chem. Soc.*, 2023, **145**, 8052–8063.
4 L. Wang, J. Y. Fan, Y. Liu, M. Y. Chen, Y. Lin, H. C. Bi, B. X. Liu, N. E. Shi, D. D. Xu, J. C. Bao and M. Han, *Adv. Funct. Mater.*, 2021, **31**, 2010912.
5 Y. H. He and G. Wu, *Acc. Mater. Res.*, 2022, **3**, 224–236.
6 H. S. Jadhav, H. A. Bandal, S. Ramakrishna and H. Kim, *Adv. Mater.*, 2022, **34**, 2107072.
7 H. F. Ma, Z. Wan, J. Li, R. X. Wu, Z. W. Zhang, B. Li, B. Zhao, Q. Qian, Y. Liu, Q. L. Xia, G. H. Guo, X. D. Duan and X. F. Duan, *Adv. Mater.*, 2019, **31**, 1900901.
8 Y. T. Luo, Z. Y. Zhang, F. N. Yang, J. Li, Z. B. Liu, W. C. Ren, S. Zhang and B. L. Liu, *Energy Environ. Sci.*, 2021, **14**, 4610–4619.
9 Y. G. Yao, Q. Dong, A. Brozena, J. Luo, J. W. Miao, M. F. Chi, C. Wang, I. G. Kevrekidis, Z. Y. J. Ren, J. Greeley, G. Wang, A. Anapolsky and L. B. Hu, *Science*, 2022, **376**, eabn3103.
10 L. F. Fan, Y. X. Ji, G. X. Wang, J. X. Chen, K. Chen, X. Liu and Z. H. Wen, *J. Am. Chem. Soc.*, 2022, **144**, 7224–7235.
11 B. Cantor, I. T. H. Chang, P. Knight and A. J. B. Vincent, *Mater. Sci. Eng., A*, 2004, **375–377**, 213–218.
12 J. W. Yeh, S. K. Chen, S. J. Lin, J. Y. Gan, T. S. Chin, T. T. Shun, C. H. Tsau and S. Y. Chang, *Adv. Eng. Mater.*, 2004, **6**, 299–303.
13 Y. T. Pan, J.-X. Liu, T.-Z. Tu, W. Z. Wang and G.-J. Zhang, *Chem. Eng. J.*, 2023, **451**, 138659.
14 L. Y. Xiao, Z. L. Wang and J. Q. Guan, *Chem. Sci.*, 2023, **14**, 12850–12868.
15 R. R. Katzbaer, F. M. D. Vieira, I. Dabo, Z. Q. Mao and R. E. Schaak, *J. Am. Chem. Soc.*, 2023, **145**, 6753–6761.
16 M. J. Cui, C. P. Yang, B. Y. Li, Q. Dong, M. L. Wu, S. Hwang, H. Xie, X. Z. Wang, G. F. Wang and L. B. Hu, *Adv. Energy Mater.*, 2020, **11**, 2002887.
17 X. W. Yu, B. Wang, C. Wang, C. Zhuang, Y. F. Yao, Z. S. Li, C. P. Wu, J. Y. Feng and Z. G. Zou, *Small*, 2021, **17**, 2103412.
18 Y. F. Ye, Q. Wang, J. Lu, C. T. Liu and Y. Yang, *Mater. Today*, 2016, **19**, 349–362.
19 J. J. Pei, T. Wang, R. Sui, X. J. Zhang, D. N. Zhou, F. J. Qin, X. Zhao, Q. H. Liu, W. S. Yan, J. C. Dong, L. R. Zheng, A. Li, J. J. Mao, W. Zhu, W. X. Chen and Z. B. Zhuang, *Energy Environ. Sci.*, 2021, **14**, 3019–3028.
20 N. N. Li, L. Sun, K. Wang, S. Xu, J. Zhang, X. X. Guo and X. H. Liu, *J. Energy Chem.*, 2020, **51**, 62–71.
21 S. S. Li, L. Wang, H. Su, A. N. Hong, Y. X. Wang, H. J. Yang, L. Ge, W. Y. Song, J. Liu, T. Y. Ma, X. H. Bu and P. Y. Feng, *Adv. Funct. Mater.*, 2022, **32**, 2200733.
22 J. Yang, D. H. Guo, S. L. Zhao, Y. Lin, R. Yang, D. D. Xu, N. E. Shi, X. S. Zhang, L. Z. Lu, Y. Q. Lan, J. C. Bao and M. Han, *Small*, 2019, **15**, 1804546.
23 L. N. Tang, Y. L. Yang, H. Q. Guo, Y. Wang, M. J. Wang, Z. Q. Liu, G. M. Yang, X. Z. Fu, Y. Luo, C. X. Jiang, Y. R. Zhao, Z. P. Shao and Y. F. Sun, *Adv. Funct. Mater.*, 2022, **32**, 2112157.
24 M. M. Zhang, H. Liu, T. J. Ma, Z. X. Song and S. Y. Shao, *Chem. Eng. J.*, 2021, **403**, 126379.
25 J. E. Li, S. Luo, B. Zhang, J. L. Lu, W. L. Liu, Q. X. Zeng, J. Wan, X. Y. Han and C. G. Hu, *Nano Energy*, 2021, **79**, 105410.

26 Y. Y. Wu, Y. Li, M. K. Yuan, H. R. Hao, X. J. San, Z. Lv, L. L. Xu and B. Wei, *Chem. Eng. J.*, 2022, **427**, 131944.
27 H. Zhang, Y. Q. Wu, X. D. Wang, C. P. Li, Z. Y. Xiao, Y. R. Liu, Y. Deng, Z. J. Li and L. Wang, *Chem. Eng. J.*, 2023, **463**, 142448.
28 C. Z. Zhong, J. X. Zhang, L. H. Zhang, Y. H. Tu, H. Y. Song, L. Du and Z. M. Cui, *ACS Energy Lett.*, 2023, **8**, 1455–1462.
29 X. T. Wang, Z. Z. Wang, Y. Li, J. T. Wang and G. K. Zhang, *Appl. Catal., B*, 2022, **319**, 121895.
30 X. Q. Mao, Y. Liu, Z. Y. Chen, Y. P. Fan and P. K. Shen, *Chem. Eng. J.*, 2022, **427**, 130742.
31 M. J. Xie, M. Zhou, Y. Zhang, C. Du, J. Chen and L. Wan, *J. Colloid Interface Sci.*, 2022, **608**, 79–89.
32 X. Xu, Y. Guo, B. P. Bloom, J. J. Wei, H. Y. Li, H. L. Li, Y. K. Du, Z. Zeng, L. Q. Li and D. H. Waldeck, *ACS Nano*, 2020, **14**, 17704–17712.
33 Y. Yamada, H. Tanaka, S. Kubo and S. Sato, *Carbon*, 2021, **185**, 342–367.
34 S.-C. Wu, Y.-H. Huang, C.-R. Liao, S.-Y. Tang, T.-Y. Yang, Y.-C. Wang, Y.-J. Yu, T.-P. Perng and Y.-L. Chueh, *Nano Energy*, 2021, **90**, 106590.
35 X.-Y. Zhang, J.-J. Wang, P. Li, Z.-Y. Tan, J.-H. Zeng, Y.-R. He and N. Habibul, *Chem. Eng. J.*, 2022, **428**, 131209.
36 H. H. Bi, X. J. He, L. Yang, H. Q. Li, B. Y. Jin and J. S. Qiu, *J. Energy Chem.*, 2022, **66**, 195–204.
37 K. Chen, S. Kim, M. Je, H. Choi, Z. C. Shi, N. Vladimir, K. H. Kim and O. L. Li, *Nano-Micro Lett.*, 2021, **13**, 60.
38 G. H. Peslherbe, *Nat. Chem.*, 2018, **10**, 899–900.
39 X. H. Wang, X. H. Wang, W. L. Tian, A. L. Meng, Z. J. Li, S. X. Li, L. Wang and G. C. Li, *Appl. Catal., B*, 2022, **303**, 120933.
40 Q. Shi, Q. Liu, Y. P. Zheng, Y. Q. Dong, L. Wang, H. T. Liu and W. Y. Yang, *Energy Environ. Mater.*, 2021, **5**, 515–523.
41 L. N. Sha, T. F. Liu, K. Ye, K. Zhu, J. Yan, J. L. Yin, G. L. Wang and D. X. Cao, *J. Mater. Chem. A*, 2020, **8**, 18055–18063.
42 S. S. Xue, S. Zhao, J. H. Lu, L. T. Wu and F. Lian, *ACS Nano*, 2022, **16**, 2651–2660.
43 S. L. Zhao, M. Li, M. Han, D. D. Xu, J. Yang, Y. Lin, N.-E. Shi, Y. N. Lu, R. Yang, B. T. Liu, Z. H. Dai and J. C. Bao, *Adv. Funct. Mater.*, 2018, **28**, 1706018.
44 M. Q. Zhao, H. R. Liu, H. W. Zhang, W. Chen, H. Q. Sun, Z. H. Wang, B. Zhang, L. Song, Y. Yang, C. Ma, Y. H. Han and W. Huang, *Energy Environ. Sci.*, 2021, **14**, 6455–6463.
45 H. Su, S. J. Song, S. S. Li, Y. Q. Gao, L. Y. Ge, W. Y. Song, T. Ma and J. Liu, *Appl. Catal., B*, 2021, **293**, 120225.
46 S. Li, L. k. Tong, Z. J. Peng, B. Zhang and X. L. Fu, *Green Chem.*, 2024, **26**, 384–395.
47 J. J. Wang, X. Y. Yue, Z. K. Xie, A. Abudula and G. Q. Guan, *Energy Storage Mater.*, 2021, **41**, 404–426.
48 L. J. Zhang, H. Jang, H. H. Liu, M. G. Kim, D. J. Yang, S. G. Liu, X. E. Liu and J. Cho, *Angew. Chem., Int. Ed.*, 2021, **60**, 18821–18829.
49 X. Luo, P. X. Ji, P. Y. Wang, R. L. Cheng, D. Chen, C. Lin, J. N. Zhang, J. W. He, Z. H. Shi, N. Li, S. Q. Xiao and S. C. Mu, *Adv. Energy Mater.*, 2020, **10**, 1903891.
50 Y. Yao, J. X. Wu, Q. X. Feng, K. Zeng, J. Wan, J. C. Zhang, B. Y. Mao, K. Hu, L. M. Chen, H. Zhang, Y. Gong, K. Yang, H. H. Zhou, Z. Y. Huang and H. X. Li, *Small*, 2023, **19**, 2302015.
51 H. Y. Xue, T. Q. Yang, Z. M. Zhang, Y. X. Zhang, Z. H. Geng and Y. He, *Appl. Catal., B*, 2023, **330**, 122641.